Materialia 9 (2020) 100598

Contents lists available at ScienceDirect

Materialia

journal homepage: www.elsevier.com/locate/mtla

Full Length Article

Shear localization and its dependence on microstructural length scales in metallic glass composites

Jonathan M. Gentile [a], Douglas D. Stauffer [b], Douglas C. Hofmann [c], Jason R. Trelewicz [a,d,*]

[a] Department of Materials Science and Chemical Engineering, Stony Brook University, Stony Brook, NY 11794, United States
[b] Bruker Nano Surfaces, Hysitron Products, Eden Prairie, MN 55344, United States
[c] Jet Propulsion Laboratory, California Institute of Technology, Pasadena, CA 91125, United States
[d] Institute for Advanced Computational Science, Stony Brook University, Stony Brook, NY 11794, United States

ARTICLE INFO

Keywords:
Metallic glass
Shear bands
Nanoindentation
Shear localization
Composite

ABSTRACT

Extrinsic approaches for the pursuit of ductility in metallic glasses have involved the introduction of a ductile crystalline phase to inhibit the propagation of a dominant shear front through the amorphous matrix material. Using nanoindentation, we explore the role of crystalline inclusions in metallic glass matrix composites with a focus on the onset of shear banding in the amorphous matrix and the nature of shear band propagation using the propensity for localization and its dependence on indentation strain rate. When indentation length scales are favorable to distribute strain to both the crystalline dendrites and amorphous matrix, we reveal a reduction in the number of detectable displacement bursts and an accompanying decrease in the magnitude of individual depth excursions from shear banding. A decrease in the stress at the onset of shear banding is also correlated with shear band trajectories interacting with the amorphous-crystalline interfaces (ACIs). Our results thus demonstrate that ACIs reducing the activation barrier for shear banding combined with dendrites arresting propagating shear fronts act to enhance the nucleation rate and in turn, promote a more homogeneous plastic response.

1. Introduction

Metallic glasses have become widely accepted as a technologically important class of materials owing to their extraordinary strength and intriguing deformation physics [1–6]. Their unique mechanical behavior derives from individual mechanistic events producing plastic strain localization into shear bands as a consequence of strain softening from local changes in the glass structure under an applied stress [7–14]. Shear bands nucleate at these locally perturbed regions in the glass through the rearrangement of atoms to accommodate shear strain, which in the context of Argon's model [7], transpires as discrete events referred to as shear transformation zones (STZs). Upon formation of an embryonic STZ cluster, free volume dilations trigger additional neighboring inelastic events [15,16], and the strain rate mismatch between the perturbed and unperturbed regions of the glass results in unimpeded growth of a dominant shear front [5,17]. Under unconstrained modes of loading (e.g. tensile loading), further accumulation of plastic strain is often concentrated on this fully developed shear band, in turn limiting macroscopic plastic strain accumulation [16]. While studies have shown that STZ activation volumes are on the order of a few to hundreds of atoms depending on the glass structure, a mature shear band may propagate millimeters in a material [5,18–20]. This disparity in mechanical length scales has plagued the search for toughening mechanisms that rely on controlling the kinetics of shear band nucleation and propagation.

The search for ductile metallic glasses has led to a number of intrinsic approaches aimed at eliminating the formation of a dominant shear front by distributing STZ activity [21–24]. The selection of alloying elements based on their elastic properties has been shown to influence short- to-medium range structural disorder and in turn, the distribution of free volume and resulting stress concentrations under an applied load [25,26]. However, compositional variations for the purpose of manipulating mechanical properties must be carefully balanced with element selection for glass formability, thus constraining the practical alloy design space. Intrinsic modulations in free volume have led to the development of metallic nanoglasses [27–29], a special class of amorphous alloys that contain nanoscale amorphous grains embedded within interfacial material of reduced density, enhanced free volume, and defective short-range ordering [30–35]. The presence of these interfacial regions distributes the process of strain localization, effectively nucleating many small shear bands rather than forming a large primary shear front [36–38], thereby promoting more homogeneous plastic flow [39–41]. Cold working a single-phase monolithic metallic glass has also been demonstrated to introduce regions of varying free volume through

* Corresponding author at: Department of Materials Science and Chemical Engineering, Stony Brook University, Stony Brook, NY 11794, United States.
E-mail address: jason.trelewicz@stonybrook.edu (J.R. Trelewicz).

https://doi.org/10.1016/j.mtla.2020.100598
Received 6 January 2020; Accepted 16 January 2020
Available online 24 January 2020

the formation of shear bands [42,43], which effectively distribute further localization to suppress shear instabilities [44].

Extrinsic approaches for enhancing homogenous plastic flow involve the introduction of a ductile crystalline phase to produce metallic glass matrix (MGM) composites, wherein strain partitioning to the ductile phase inhibits the propagation of a dominant shear front through the amorphous matrix material [45–48]. *Ex situ* techniques have involved both partial devitrification of as-solidified amorphous alloys and dispersing preformed crystallites within a melt prior to solidification [49–59]. The resulting inclusions are typically nanocrystalline with performance influenced by their size, distribution, and mechanical properties [51,52,60–62]. For example, STZ activity has been shown to be more distributed in the presence of nanocrystalline inclusions, but for shear band propagation to be affected, the inclusions must be larger in size and more compliant relative to the amorphous matrix [61]. The introduction of a crystalline phase instead through dendritic solidification (often referred to as *in situ* composites) has also produced improvements in tensile ductility and attributed to the intrinsically larger length scales of the crystalline dendrites limiting propagation of a dominant shear front [63–68]. Similar behavior has been observed in laser welds of a Zr-based glass to bulk Ti, where microcantilever testing of the glass/Ti fusion zone revealed that the formation of compliant Zr-rich particles distributed the process of shear localization [69]. Additionally, MGM composites containing phase transformable crystalline dendrites have shown to further enhance the measured elongation to failure, which simultaneously enables more sophisticated pathways for plastic strain accommodation [70,71]. While the mechanical length scales associated with shear banding in the amorphous matrix spans two orders of magnitude (1–100 μm), only the characteristic size of the primary shear bands have been shown to be comparable to the size and spacing of the dendrites [72]. This dependence of mechanical performance on effective length scale matching implies that microstructural features can be deliberately tailored on the basis of the dominant deformation mechanisms for promoting a transition to homogeneous plastic flow.

The aforementioned examples were solely for the addition of a soft percolated crystalline phase within a harder amorphous matrix material. If instead a brittle reinforcement phase is introduced within the amorphous matrix, the propensity for brittle fracture of the composite has been shown to be enhanced through undisrupted propagation of a dominant shear front [73]. Several studies have postulated that catastrophic shear runaway is inhibited by geometrical constraints the crystalline inclusions place on shear band propagation [45,74]; however, uninhibited propagation of shear bands through a brittle crystalline phase indicates that strain energy dissipation through plasticity is also critical to arresting shear bands initiated in the amorphous matrix. Others have suggested that the softer inclusion phase deforms preferentially prior to the onset of plasticity in the amorphous matrix, which in turn produces stress concentrations at the boundaries that promote strain distribution throughout the composite [49]. These observations, while critical to our current understanding of the interaction of shear bands with crystalline inclusions, have been largely inferred from post-mortem microstructural analysis, making it difficult to assess the role of competing (and even complementary) deformation processes during plastic strain accumulation in MGM composites.

In this paper, we employ instrumented nanoindentation to study the deformation behavior of MGM composites where the crystalline phase was introduced *in situ* through dendritic solidification. Our primary focus is to understand the influence of the crystalline dendrites on the deformation physics of the amorphous matrix by quantitatively mapping the crossover from the mechanical response of the individual phases to a combined phase response where the amorphous-crystalline interfaces (ACIs) impact the process of shear localization. In composites with varying crystalline phase fractions, the role of stress state in shear band nucleation is quantified as a function of the governing microstructural length scales to explore the role of amorphous- crystalline interfaces (ACIs) in the onset of plasticity. We then outline the transition from discrete to continuous deformation by measuring the fraction of discrete plastic events as a function of indentation strain rate in the different length scale composites. A confluence of effects involving enhanced shear band nucleation at ACIs, preferential strain accommodation in the crystalline dendrites, and the arrestment of propagating shear fronts at the ACIs are demonstrated to govern the mechanical behavior of MGM composites with the transition from localized to homogenous flow depending largely on the underlying microstructural characteristics.

2. Experimental methods

Metallic glass matrix composites containing *in situ* solidified dendrites were synthesized through arc melting pure elements followed by suction casting in an Argon atmosphere. The nominal compositions of the amorphous matrix and crystalline dendrites were $Zr_{31–34}Ti_{17–22}Nb_{1–2}Cu_{9–13}Be_{31–38}$ and $Zr_{40–44}Ti_{42–45}Nb_{11–14}Cu_{1–3}$, respectively, where concentrations are specified in atomic percent. Following Hofmann et al. [72], the dendritic volume fraction was controlled by varying the beryllium concentration while maintaining mutual ratios of the constituent elements in an effort to minimize effects due to large variations in compositions. The following alloys with crystalline phase volume fractions of 47%, 53%, and 61%, respectively, were produced for this study: $Zr_{36.6}Ti_{31.4}Nb_{7.0}Cu_{5.9}Be_{19.1}$, $Zr_{38.3}Ti_{32.9}Nb_{7.3}Cu_{6.2}Be_{15.3}$, and $Zr_{39.6}Ti_{33.9}Nb_{7.6}Cu_{6.4}Be_{12.5}$. We note that subtle modulations in composition are expected within the dendrites and the amorphous matrix in the different alloys due to differences in the solidification behavior. However, as we will show, our backscatter SEM analysis indicates that compositional variations across each respective phase were minimal and within the resolution of this technique. A monolithic amorphous alloy with a nominally equivalent composition to the amorphous matrix material was also produced and referred to herein as the bulk metallic glass (BMG) sample.

Sections were extracted from the bulk ingots for nanomechanical testing, mounted in epoxy and adhered to nickel-plated neodymium magnets using cyanoacrylate adhesive, and polished to a mirror finish using standard metallurgical techniques with the final polishing step employing 0.01 μm colloidal silica. Quantitative analysis of the dendrite morphology and characteristic length scales was accomplished using a JEOL7600F scanning electron microscope (SEM) in the Center for Functional Nanomaterials at Brookhaven National Laboratory. Two separate sets of nanoindentation experiments were performed to correlate microstructural length scales with mechanical properties, including through-thickness measurements and two-dimensional surface mapping. In addition, Hertzian contact and shear banding statistics experiments were performed to study the influence of ACIs and crystalline dendrites on the nucleation and propagation of shear bands in the amorphous matrix.

Mechanical property measurements as a function of contact depth were accomplished using a Hysitron TS75 Triboscope lateral force transducer coupled to a Bruker Dimension Icon AFM, which contains z-axis load and depth resolutions of 0.1 μN and 0.2 nm, respectively. Experiments were conducted at room temperature and to minimize thermal drift, the probe tip was placed in contact with the specimen surface for at least one hour prior to testing. Instrumental drift was characterized during the linear unloading segment using a 10 s hold at 10% of the maximum load. A 150 nm diamond Berkovich probe was employed for measurement of through-thickness mechanical properties with indents centered deliberately on each phase of the composite, and its area function was calibrated on fused silica within a contact depth range of 50–150 nm. The indentation strain rate was held constant at 0.5 s^{-1} to maximum loads ranging between 2mN and 10mN, which produced contact depths between 60 and 260 nm. Although the actual contact depths exceeded the calibrated range on fused silica in some tests, they remained consistent with measurements collected at lower depths, thereby indicating the probe geometry was invariant in all our experiments beyond the calibrated range of the area function. Indent spacing was estab-

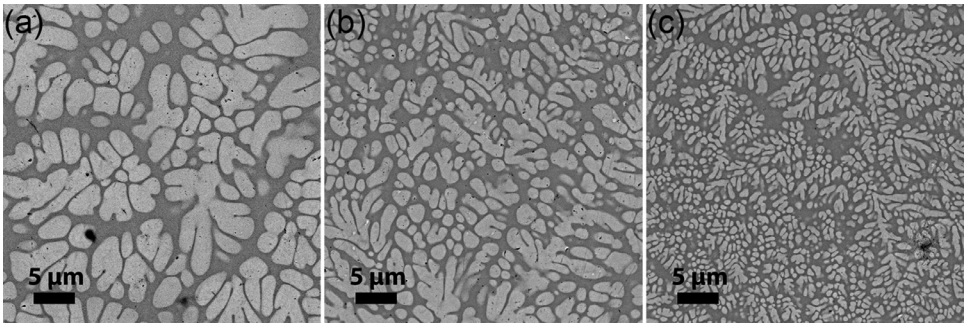

Fig. 1. Backscatter SEM images for the three MGM composites including (a) MGM-12Be, (b) MGM-15Be, and (c) MGM-19Be. These micrographs qualitatively demonstrate the inherent connection between the crystalline phase fraction and characteristic length scales of the composite microstructures.

lished using the residual impression areas, which were estimated for the different geometry probes to produce a distribution of the impression widths. Based on the extreme values from these distributions, a minimum center-to-center spacing of 10 μm was employed to ensure the peripheries of adjacent indents were never within 5 μm of each other at the maximum indentation load. A minimum of 15 indents with negligible drift were acquired per condition for statistical analysis of hardness and reduced modulus, which were determined using the Oliver and Pharr method [75].

For the development of high-resolution property maps, we used a TI980 TriboIndenter operated in XPM (accelerated property mapping) mode [76]. A diamond cube corner probe was employed based on its ability to impart larger localized plastic strain at lower contact depths relative to the Berkovich probe, thus enabling higher spatial resolution for property mapping. An array of 625 indents was placed within a 10×10 μm^2 scan window on each composite microstructure using a constant loading rate of 2 mN/s to a maximum load of 0.2 mN with resultant contact depths between 10 and 25 nm. Mechanical properties were extracted for each indent using the same methodology outlined for the Berkovich probe and recorded as a function of lateral position within the scan window.

Instrumented Hertzian contact experiments were performed using the Hysitron TS75 Triboscope to quantify the load associated with the first distinguishable shear band event, which manifests as a displacement burst or "pop-in" event during loading. To provide a well-defined stress field during elastic contact, diamond conospherical probes of radii 0.5, 2.0, and 5.0 μm were loaded at a constant loading rate of 0.15 mN/s to a maximum specified load, producing indentation depths such that the probe geometry may be approximated as spherical [77]. The load at first pop- in was identified following the methods introduced by Packard and Schuh [78], where a pop-in is identified as a sudden spike in the indentation velocity with a minimum of 100 indents used in the analysis for statistical significance. The propensity for shear localization, defined as the fraction of discrete to total plasticity during the indentation loading cycle, was quantified as a function of indentation loading rate separately on the amorphous matrix and dendritic phases of the composites with behavior compared to the BMG sample. The 0.5, 2.0, and 5.0 μm diamond conospherical probes were used to vary the plastic zone size with indentation loading rate spanning four orders of magnitude from 0.1 to 100 mN/s to a maximum load of 10 mN. Both the load at first pop-in and propensity for shear localization were analyzed using custom scripts developed in Matlab.

3. Microstructure and mechanical property correlations

From the perspective of the amorphous matrix material, the presence of crystalline dendrites introduces interfaces that can serve as preferred nucleation sites for the activation of STZs, which in turn would reduce the activation barrier for the onset of shear banding. However, strain partitioning to the softer dendritic phase will simultaneously influence the composite response, making it difficult to assess the role of interfaces on the shear localization behavior in the amorphous phase. The intrinsic connection between dendrite volume fraction, size, and spacing [72] provides an opportunity to probe the transition from individual phase behavior to the effective response of the composite microstructure where plasticity in one phase becomes influenced by the other. In this section, we quantify this transition by mapping the mechanical properties of the individual phases as a function of contact depth using nanoindentation and establish correlations between the scaling of properties and underlying length scales of the composite microstructure.

Representative backscatter SEM micrographs for each MGM composite sample are shown in Fig. 1 organized from (a)–(c) based on Be content as reflected in the sample nomenclature, i.e., MGM-(12,15,19)Be where the Be concentration is in atomic percent. The marked phase contrast was due to the crystalline dendrites being nominally free of Be, which instead resides in the amorphous phase [72]. An increase in the Be content generally produced finer composite microstructures, though its impact on the volume fraction of the respective phases was not immediately apparent from qualitative imaging. Quantitative analysis was conducted to map the length scale dependence of the composite microstructural features as a function of the primary control variable, the Be concentration. Due to the variations in dendrite size and shape across the different samples, a universal length scale is difficult to define for both the crystalline reinforcements (e.g., length, aspect ratio, etc.) and amorphous matrix (e.g., interdendritic spacing). For the former, we approximated the dendrites as spherical and employed the dendrite radius as the characteristic length scale. Since this approximation does not apply to the percolating amorphous phase, we instead adopted the approach described by Cheng et al. [79] to infer three- dimensional microstructural characteristics from a two-dimensional micrograph. In particular, the interfacial area per unit volume was estimated from the total phase boundary length within a prescribed area, which was directly measured from the micrographs. The inverse of this specific interfacial area is representative of the average distance between interfaces or interdendritic spacing, thus providing a measurable characteristic length scale for the amorphous matrix.

The dendrite radius and volume fraction shown as a function of Be concentration in Fig. 2a scaled inversely with the amount of Be, aligning with prior measurements on similar MGM composite microstructures [72,79]. An increase in Be concentration therefore produced a decrease in the dendritic volume fraction, which was accompanied by a reduction in dendrite radius from 1.76 to 0.43 μm. The characteristic length scale of the amorphous matrix also decreased with increasing Be concentration in Fig. 2b from 1.37 to 0.43 μm, but was instead accompanied by an increase in volume fraction. As summarized in Table 1, the MGM composites containing less Be exhibited larger crystalline phase fractions and microstructural length scales. Increasing the Be concentration produced finer microstructural length scales with phase distributions that converged to approximately 50% by volume fraction.

Indentation hardness was mapped on the different MGM composite microstructures as shown in Fig. 3 as a function of increasing Be concentration from (a)–(c) including the scanning probe micrographs on the left and corresponding hardness maps on the right with values normalized by the average hardness of the softer dendritic phase. The

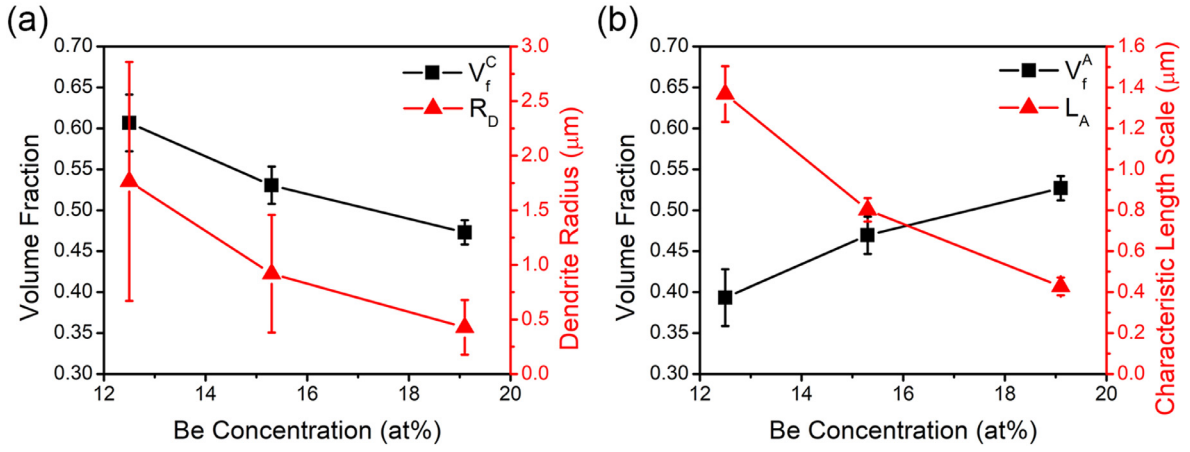

Fig. 2. Microstructural characteristics of the MGM composites as a function of the Be concentration including (a) crystalline phase fraction, V_f^C, and average dendrite radius, R_D, and (b) amorphous phase fraction, V_f^A, and characteristic length scale of the amorphous matrix, L_A.

Table 1
Sample designations for the MGM composites and corresponding microstructural characteristics measured for the crystalline dendrites and amorphous matrix. The composites are organized in order of increasing crystalline phase fraction (and thus decreasing Be concentration) with the BMG sample included for reference.

Sample designation	Be content (at%)	Crystalline dendrites		Amorphous matrix		
		Volume fraction V_f^c	Dendrite radius R_D (μm)	Volume fraction V_f^A	Interfacial density L_A^{-1} (μm^{-1})	Characteristic length scale L_A (μm)
MGM-19Be	19.1	0.47	0.43	0.53	2.36	0.43
MGM-15Be	15.3	0.53	0.92	0.47	1.25	0.80
MGM-12Be	12.5	0.61	1.76	0.39	0.74	1.37
BMG	34.0	0.00	N/A	1.00	N/A	N/A

apparent hardness difference between the two phases was most pronounced in the MGM-12Be sample, where the hardness of the amorphous matrix was nearly double that of the dendrites and exhibited a sharp gradient from the central regions of the amorphous matrix to the phase boundaries. This distinct behavior of the two phases remained evident for the MGM-15Be sample in Fig. 3b, but with more subtle hardness gradients in the amorphous regions that also became evident at the edges of the dendrites near the amorphous-crystalline interfaces (ACIs). The hardness of the two phases eventually became indistinguishable in Fig. 3c and converged on the average value of the crystalline dendrites in the MGM-19Be sample, which contained nominally equivalent phase fractions with finer microstructural length scales. This convergence was attributed to the plastic zone interacting with both phases simultaneously as the microstructural length scales were reduced with increasing Be concentration. Similarly, the hardness gradients present in the individual phases of MGM-12Be and MGM-15Be were due to sampling a combined phase response near the interfaces where the plastic zone encompassed both phases of the composites rather than intrinsic changes specific to either phase of the composite.

To capture the transition from individual phase behavior to a combined phase mechanical response and its dependence on the microstructural length scales, indentation hardness and reduced modulus were mapped as a function of contact depth. Results are shown in Fig. 4 with data delineated for indents deliberately placed on the amorphous phase (MGM/AP) and crystalline phase (MGM/CP); trends are also included for the BMG in the upper panels with average values represented by the dashed lines in all panels. The decrease in hardness with contact depth for the BMG is attributed to strain softening during shear band formation within the expanding plastic zone, which is consistent with a number of reports from literature [80–83] and thus not simply due to measurement artifacts from, e.g., pile-up. Hardness values acquired on the amorphous phase of the MGM-12Be sample in the upper panel of Fig. 4a were shifted to subtly lower values, but did not converge to the significantly lower hardness of ~4 GPa for the dendrites. The trend with contact depth was analogous to the BMG, indicating that the hardness difference was due to intrinsic characteristics of the amorphous matrix rather than biasing of the shear banding process by ACIs. This is substantiated by the depth-independent reduced modulus values for the amorphous matrix in Fig. 4b, although some degree of reduction relative to the BMG could be due to long-range elastic interactions with the dendrites. With maximum contact depths of 200 and 270 nm corresponding to less than 15% the length scales of both the amorphous matrix and dendrites, the plastic zone developed solely within each phase, thus confirming the responses were reflective of individual phase behavior in MGM-12Be.

The reduction in microstructural length scales accompanying the increase in Be concentration shown in Fig. 2 resulted in the MGM-15Be composite exhibiting transitional behavior while the MGM-19Be composite converged to a combined phase response. At contact depths below 120 nm in the MGM-15Be sample, we observed a similar indentation size effect for the amorphous phase in the MGM/AP hardness trend shown in the middle panel of Fig. 4a with an identical modulus to the MGM-12Be sample in Fig. 4b. The excellent agreement in the mechanical properties of these two alloys at low contact depths also confirms that subtle compositional differences have no discernible impact on the individual phase mechanical response. The subsequent shift in slope in the MGM/AP hardness trend above 150 nm and resultant decrease in hardness toward the MGM/CP trend combined with the convergence in the reduced modulus indicate that the behavior was reflective of the combined phase response at larger indentation depths. This transition depth of 150 nm represents 20% the characteristic length scale of ~750 nm

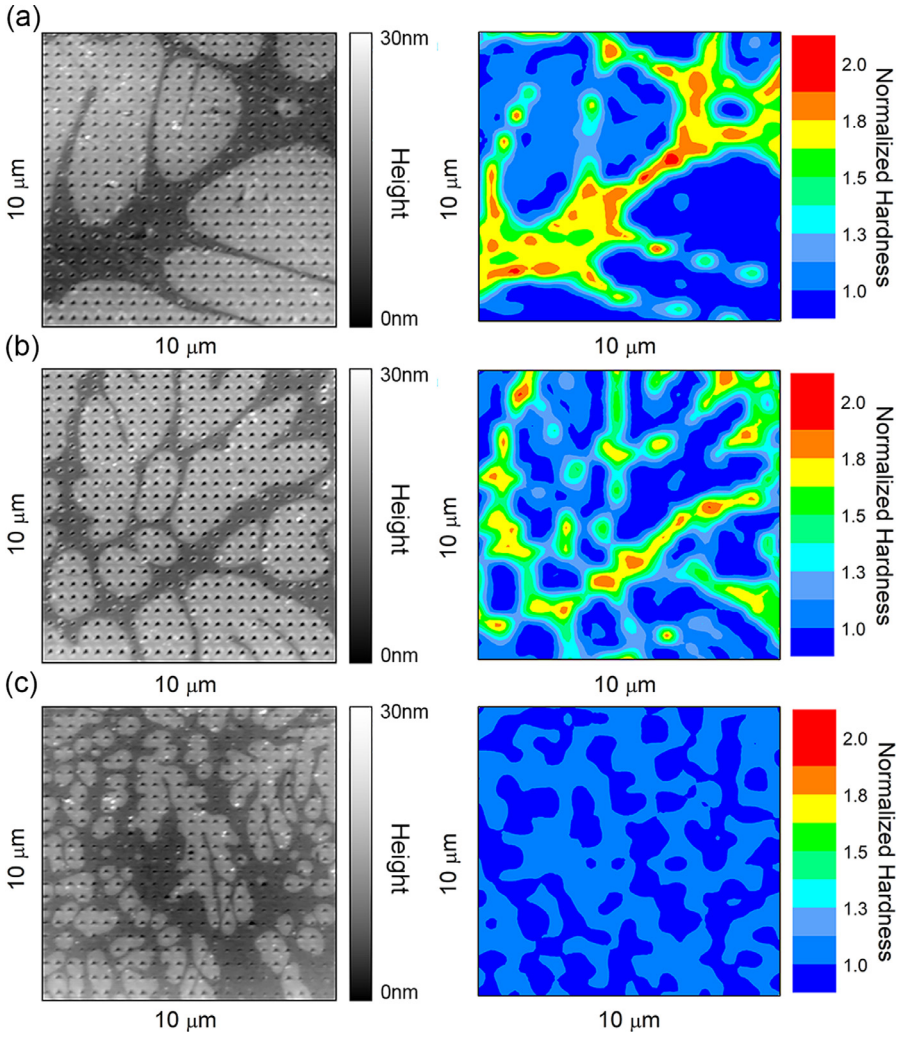

Fig. 3. Scanning probe micrographs and corresponding indentation hardness maps for (a) MGM-12Be, (b) MGM-15Be, and (c) MGM-19Be. The larger microstructural length scales evident in (a) enabled the individual phase mechanical properties to be quantified, which manifested as a larger disparity in the hardness of the crystalline dendrites and amorphous matrix. As the length scales of the composites were refined through the addition of Be, the hardness of the two phases converged from (b) to (c), which was indicative of the combined phase mechanical response.

for the amorphous matrix in the MGM-15Be sample from Fig. 2b. The further decrease in the length scales of both phases to approximately 400 nm in the MGM-19Be sample shifted this transition to lower contact depths with only a subtle disparity in hardness detected below 100 nm in the bottom panel of Fig. 4a corresponding to 40% the microstructural length scales. Identical moduli trends in Fig. 4b, which were governed by the stiffer amorphous matrix up to ~150 nm with only a marginal reduction at larger contact depths, confirm the mechanical response of the MGM-19Be sample was representative of the combined phase behavior across the full range of contact depths.

An important caveat to note is that our nanoindentation results are not representative of a true composite response since the size of the plastic zone is insufficient to sample effects from the fully interconnected composite microstructure. The differences between a combined phase and full composite mechanical response can be understood by considering the measured hardness values relative to rule-of-mixtures predictions. The convergence in hardness reported here aligns with a rule-of-mixtures prediction calculated using the hardness values and relative volume fractions of the individual phases. Conversely, microindentation experiments performed by Narayan et al. [84], where the much larger plastic zone indeed sampled composite network effects, demonstrated that the hardness of the composite exceeded rule-of-mixtures predictions due to the harder amorphous matrix constraining deformation of the softer dendrites. We emphasize that our results are consistent with this finding since we are instead sampling the *combined phase response* from a plastic zone sampling the collective behavior of the amorphous matrix and crystalline dendrites, but not the connectivity effects of the full composite microstructure.

4. The onset of shear banding in the presence of ACIs

Recognizing that deformation is accommodated by STZ plasticity in the amorphous matrix and dislocation slip in the dendrites [85–87], the transition from individual to combined phase responses will inherently be accompanied by a coupling of the disparate mechanisms across the ACIs. The length scales of the microstructure relative to the size of the plastic zone governed this transition, which confirms the reduction in hardness contrast in Fig. 3(a–c) was due to sampling of the combined phase mechanical response rather than deriving from intrinsic changes in either phase of the composites. We can thus leverage our control over the plastic zone size relative to the different microstructural length scales to quantify the impact of the ACIs on the shear banding kinetics in the amorphous matrix and understand its implications for the delocalization of plastic strain. In this section, we present a comprehensive analysis of the onset of incipient plasticity in the amorphous matrix using the MGM-12Be and MGM-19Be samples, which exhibited individual and combined phase responses, respectively. The state of stress beneath the indenter is manipulated using different radii conospherical probes with the first shear band event identified as a function of probe radius and correlated to the length scale of the microstructure using the shear plane stress criterion.

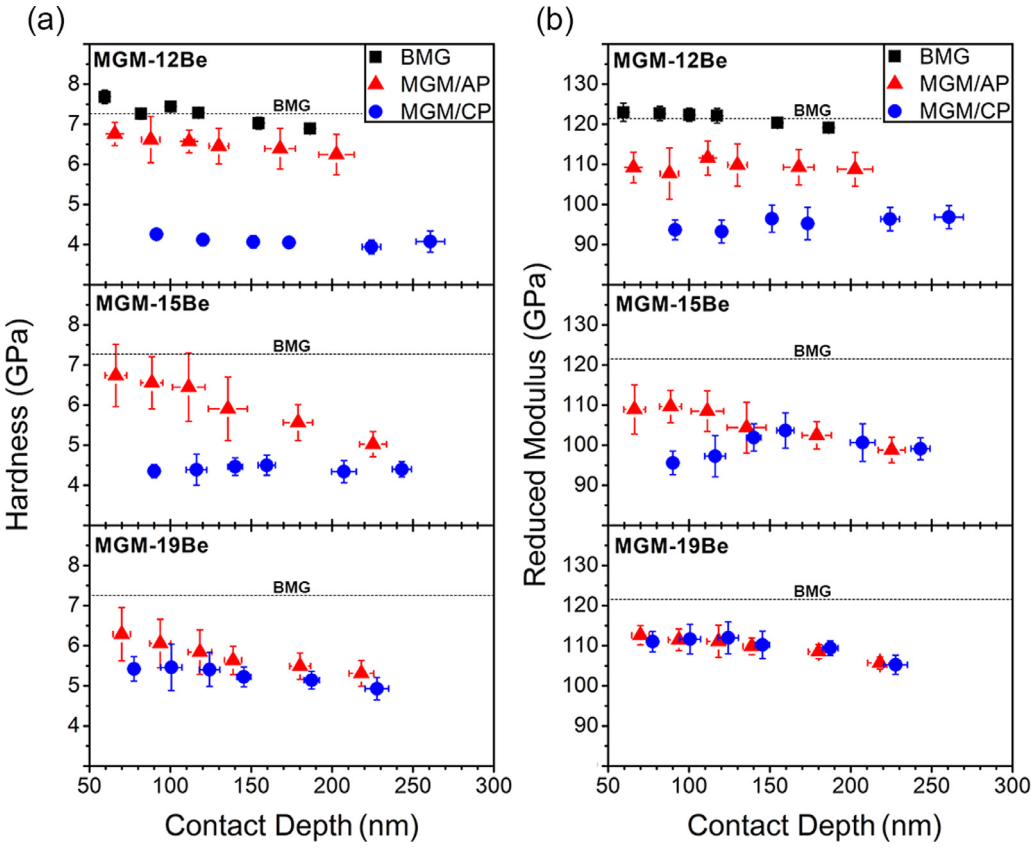

Fig. 4. (a) Indentation hardness and (b) reduced modulus as a function of contact depth for the three MGM composites arranged in order of increasing Be concentration (and thus decreasing microstructural length scales) from the upper to lower panels. Data for the BMG is plotted in the upper panel with average values included on all graphs for reference. The convergence in mechanical properties for the amorphous (MGM/AP) and crystalline (MGM/CP) phases signaled a transition from the individual phase to combined phase mechanical response.

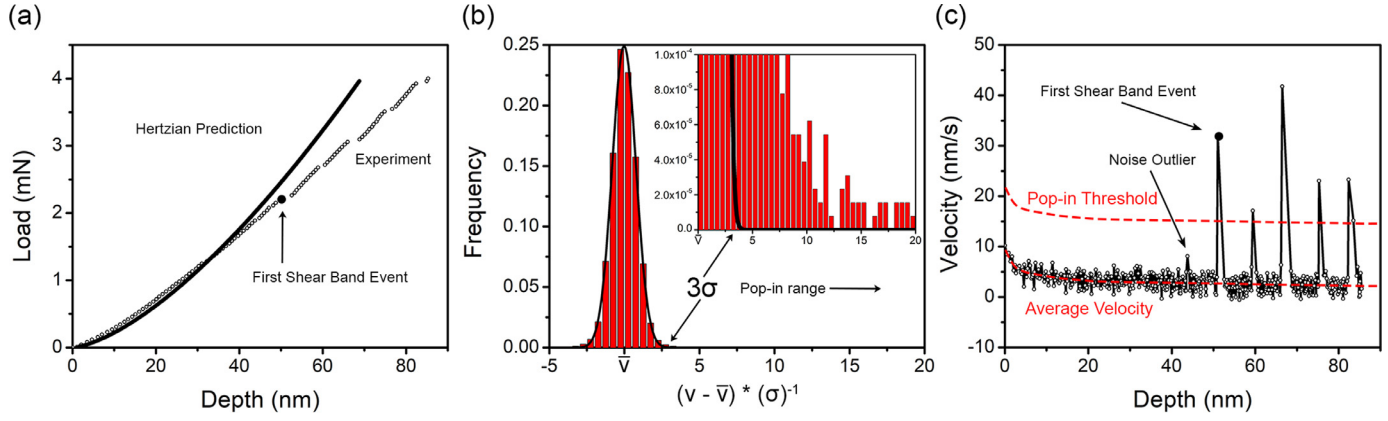

Fig. 5. (a) Illustrative load-displacement curve relative to the Herztian prediction for the MGM- 12Be composite demonstrating the first shear banding event. (b) Corresponding velocity histogram collapsed into a standard normal distribution from which the threshold was established to identify the load at first pop-in. (c) Application of the pop-in threshold to the indentation velocity data determined from (a) demonstrating the distinction between true pop-in events and noise outliers.

A representative analysis for the first pop-in event is illustrated in Fig. 5 for a single loading curve acquired from an indent placed on the amorphous matrix of the MGM-12Be composite. The first displacement burst is evident in Fig. 5a as a clear departure from the Hertzian prediction at a contact depth of ~50 nm and as with monolithic metallic glasses, was followed by a series of pop-ins corresponding to the activation of multiple shear banding events [88]. To quantify shear banding behavior through the identification of pop-ins in the indentation velocity profile, a velocity peak threshold was established to capture the transition from instrumentation noise (e.g., due to acoustic vibrations) to indentation events that derive from discrete deformation events. Velocity histograms, as shown in Fig. 5b for the MGM-12Be sample, were employed with data represented as the difference in the instantaneous velocity, v, and the average velocity, $\bar{v}$, normalized by the standard deviation of the data set, σ. By fitting only the noise distribution, its tails were observed to terminate at approximately 3 σ, and thus velocity spikes exceeding this threshold value as shown in the inset of Fig. 5b were categorized as displacement bursts deriving from shear band events.

Application of this established noise amplitude range to a velocity data set as a function of depth from a single indent is shown in Fig. 5c.

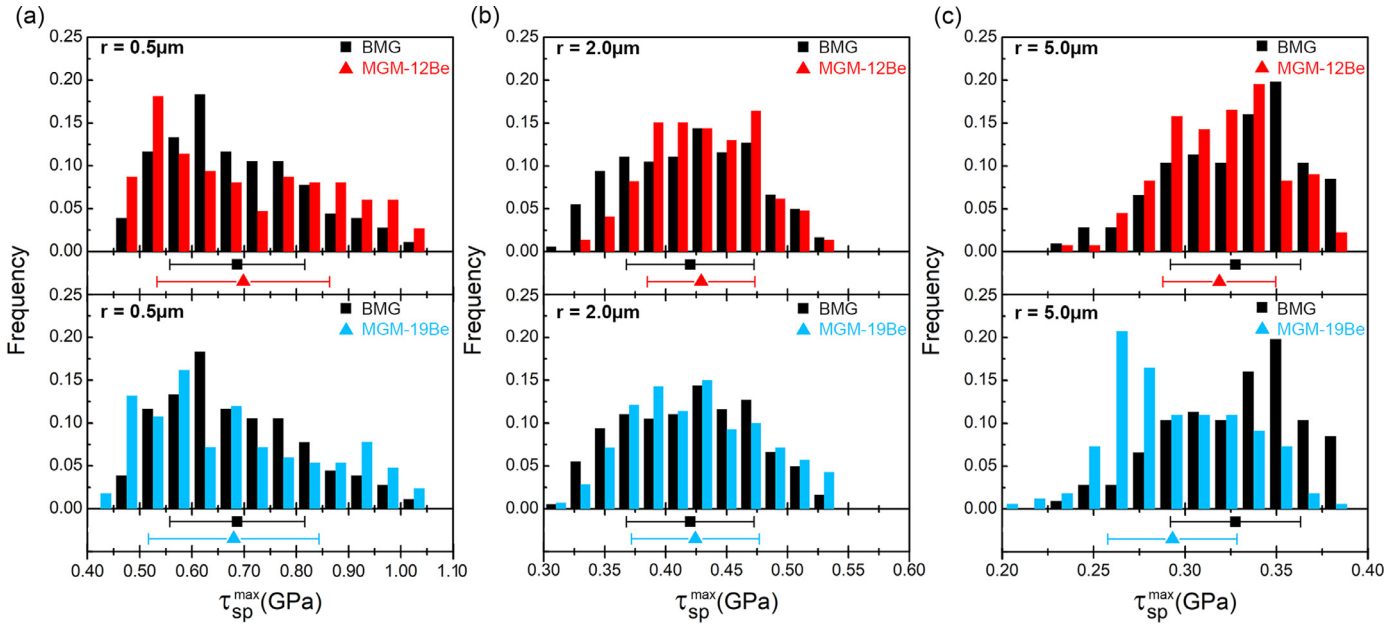

Fig. 6. Distributions for the maximum shear plane stress with corresponding mean values shown below the histograms for the MGM-12Be and MGM-19Be composites relative to the BMG for probe radii of (a) 0.5, (b) 2.0, and (c) 5.0 μm. The shift in the average $\tau_{sp}max$ for the latter probe is accompanied by a discernible shift in the overall distribution to lower values of $\tau_{sp}max$.

Velocity bursts from shear banding events are conspicuously evident relative to both the average noise range and subtle outliers as indicated on the plot. This procedure was applied to each indentation loading curve for the development of statistical distributions for the load at first pop-in to identify the onset of incipient plasticity.

To evaluate the stress state at the onset of incipient plasticity from the loads at first pop-in, we implemented the shear plane yield criterion [78], which defines a preferred shear plane for yielding as the trajectory that sustains stresses exceeding the yield stress along its entire path (as opposed to, e.g., a maximum shear stress criterion). Calculation of the maximum shear plane stresses, τ_{sp}^{max}, was accomplished using elastic constants for the amorphous matrix determined from the reduced modulus data for the MGM-12Be sample (i.e., the upper panel of Fig. 4b), Poisson's ratio from Hofmann et al. [72], and the loads at first pop-in from each indentation dataset. Distributions for the maximum shear plane stresses are shown for the MGM-12Be and MGM- 19Be samples relative to the BMG as a function of probe radius in Fig. 6(a–c), respectively, with average values and standard deviation plotted below the histograms.

Consistent across all the samples was a decrease in stress required to initiate shear banding with increasing probe radius (note the different *x*-axis scaling), which is consistent with previous observations for Zr-based metallic glasses [78] and attributed to a more distributed stress field sampling a larger fluctuations in topological ordering [5,89,90]. The scaling behavior for the MGM-12Be sample in Fig. 6(a–c) was identical to the BMG, indicating that either: (i) the presence of ACIs did not influence the shear band nucleation kinetics in the amorphous matrix, or (ii) ACIs were not within the plastic zone at the stresses corresponding to the first pop-in event on this sample. The results in Fig. 4 for the MGM-12Be sample suggest the latter since the Berkovich indents, which produced fully-developed plastic zones, were not influenced by the presence of the crystalline phase and thus captured the individual phase response of amorphous matrix. The stress distributions at first pop-in for the MGM-19Be sample also aligned with the BMG for the two smaller probes. However, for the largest probe radius of 5 μm, the distribution decidedly shifted to lower values of τ_{sp}^{max} in Fig. 6c, which was reflected as a reduction in the average stress for the first pop-in event relative to the BMG. From Fig. 4b, the mutually consistent reduced modulus for Berkovich indents on the amorphous matrix and crystalline dendrites suggests this difference derived from the ACIs influencing the onset of incipient plasticity in the MGM-19Be sample.

The relationship between the stress at first pop-in and composite length scales was explored through mapping of the entire shear plane trajectories corresponding to the average τ_{sp}^{max} for both composites in Fig. 6 as a function of probe radius. The compiled shear plane stress fields are plotted in an elastic half-space and superimposed over representative backscatter SEM micrographs for the MGM-12Be and MGM-19Be samples in Figs. 7 and 8, respectively; axes apply to both the stress contours and micrographs. Common to both samples was the probe size dependence, where increasing the probe radius produced shear plane stresses that became less localized and evolved to larger depths within the amorphous matrix. The magnitude of the sustained stress along the preferred trajectory of ~0.06·P_m, where P_m is the mean indentation pressure, was also consistent across the two composites and in good agreement with the shear plane stress reported by Packard and Schuh [78].

Interaction of the shear path with the ACIs was governed by the interplay between the mechanical length scales produced from the different probe sizes and microstructural characteristics of the two composites. As shown in Fig. 7a for the MGM-12Be sample, the smallest probe radius of 0.5 μm produced a highly localized shear path extending only 0.25 μm into the amorphous matrix. Increasing the probe size expanded the depth of the shear path trajectory with the stress field generated by 5.0 μm probe extending 1.3 μm into the material. The representative SEM micrograph in Fig. 7c qualitatively suggests that for indents deliberately placed on the amorphous matrix, this average shear path depth would not produce a stress field with a τ_{sp}^{max} trajectory that would interact with the ACIs. Quantitative evidence is provided by the microstructural data in Fig. 2b, where the characteristic microstructural length scale of 1.4 μm for the amorphous matrix in this sample was just beyond the maximum depth of the stress field. Collectively, these results demonstrate that the ACIs did not influence the onset of shear banding in the MGM-12Be sample, thus accounting for close alignment between the MGM-12Be composite and BMG stress distributions in the upper panels of Fig. 6(a–c).

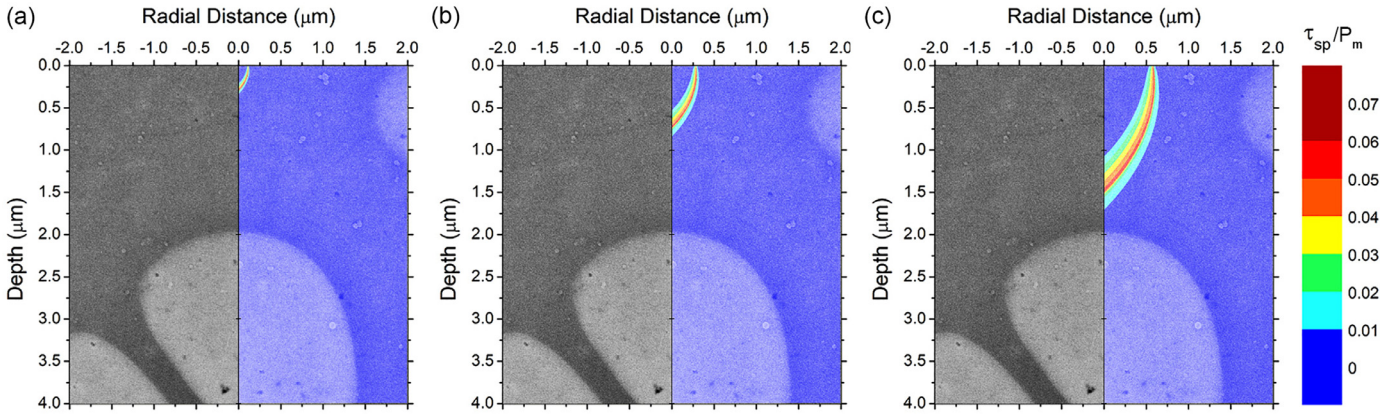

Fig. 7. Shear plane stresses, τ_{sp}, in the amorphous matrix of the MGM-12Be composite at the critical loads for shear band nucleation for the (a) 0.5, (b) 2.0, and (c) 5.0 μm probes superimposed over a representative SEM micrograph. For the selected conditions where the depth of the depicted dendrite aligned with the characteristic length scale of the amorphous matrix, the shear trajectory did not interact with the crystalline phase.

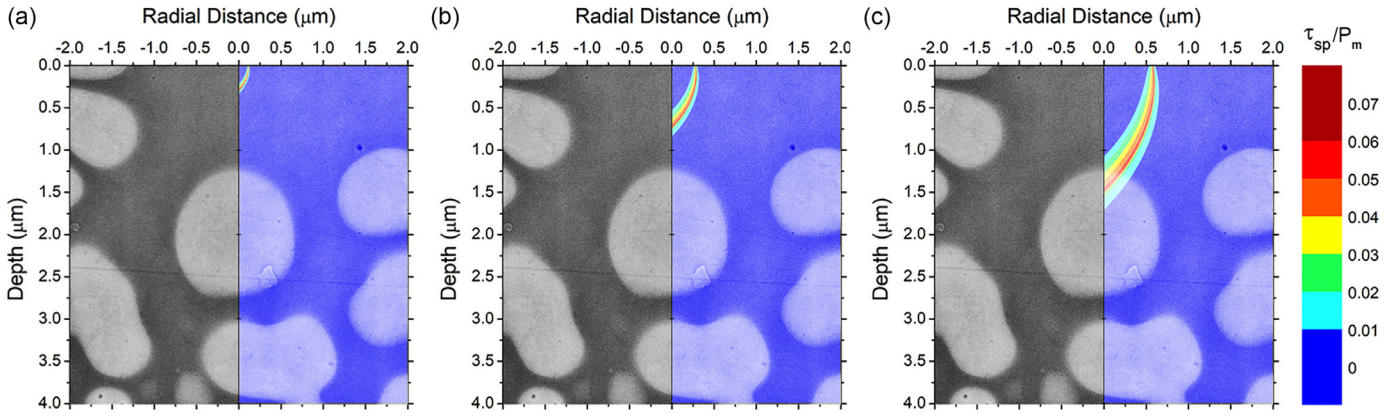

Fig. 8. Shear plane stresses, τ_{sp}, in the amorphous matrix of the MGM-19Be composite at the critical loads for shear band nucleation for the (a) 0.5, (b) 2.0, and (c) 5.0 μm probes superimposed over a representative SEM micrograph. The shear trajectory intersected with a crystalline dendrite for the largest probe size of 5.0 μm and consistent with the reduction in the load at first pop-in observed for these conditions.

Evolution of the shear plane stresses with probe radius in the MGM-19Be sample produced stress fields that eventually overlapped with the ACIs in Fig. 8(a–c). Although the SEM micrograph is only representative of the microstructure, this result is substantiated by the smaller characteristic length scale of approximately 0.4 μm in Fig. 2b for the amorphous matrix, which was well within the depth of the shear band path for the largest probe size. Thus, the mechanical length scales produced by the 5.0 μm probe combined with the fine microstructure of the MGM- 19Be composite produced favorable conditions for the onset of shear banding in the lower panel of Fig. 6c to be influenced by the ACIs. The reduction in the shear plane stress is indicative of a reduced activation barrier for the nucleation of shear bands and consistent with the findings of Hofmann et al. [72], where enhancements in tensile ductility were attributed to the mechanically soft crystalline inclusions favoring the distributed nucleation of shear bands at ACIs. Finally, we note that under localized mechanical testing configurations such as nanoindentation, only certain testing conditions will sample the effect of ACIs on plasticity, specifically when the plastic zone size aligns with the microstructural length scales of the composite.

5. Implications for the transition from incipient to homogenous flow

In MGM composites where plastic strain ultimately partitions between the stiffer amorphous matrix and more ductile crystalline dendrites, enhanced shear band nucleation kinetics in the presence of the ACIs will impact the amount of strain accommodated through discrete plastic flow. Shear band propagation will also be influenced by the presence of the dendrites, particularly through the coupling of the shear front with dislocation plasticity across the ACIs. In this section, we probe the competition between shear band nucleation and propagation in the amorphous matrix during the formation of a fully-developed plastic zone by mapping the propensity for localization in the MGM-12Be and MGM-19Be composites relative to the BMG. We consider indentation responses from distinct probing of the amorphous and crystalline phases of the composites to decouple the mechanical and microstructural length scale effects. Flow transitions are ultimately rationalized in the context of the microstructural length scales using the fraction of discrete plasticity, number of shear banding events, and insights from previous sections.

Defined as the fraction of discrete plasticity during indentation, the propensity for localization was calculated as the sum of the depth excursions from shear banding, h_i^{SB}, normalized by the total residual plastic depth, $h_{plastic}$, to a constant maximum load of 10 mN. The respective inputs for this calculation are illustrated on the loading curve in Fig. 9a from representative data acquired on the MGM-12Be sample using a 2.0 μm probe. Pop-in events were identified using a similar procedure to Section 4, but modified to capture shear banding events during the entire loading cycle used in generating a fully-developed plastic zone. The effect of probe radius is shown in Fig. 9b for indents produced solely on the amorphous phase of the MGM- 12Be sample. Assuming the strain for a spherical probe is captured by $0.2a/R$ where a is the contact radius

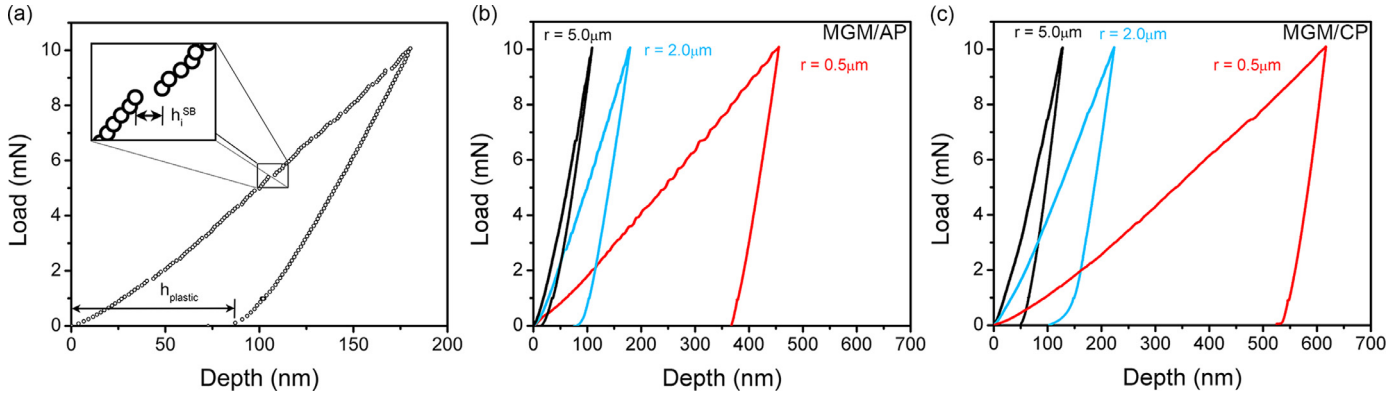

Fig. 9. (a) Illustrative determination of the fraction of discrete plasticity using incremental depth excursions from each shear banding event; representative data shown for the MGM-12Be sample indented with a 2.0 μm probe. The effect of probe radius on the MGM-12Be composite for indents placed deliberately on (b) the amorphous matrix (MGM/AP) and (c) the crystalline dendrites (MGM/CP).

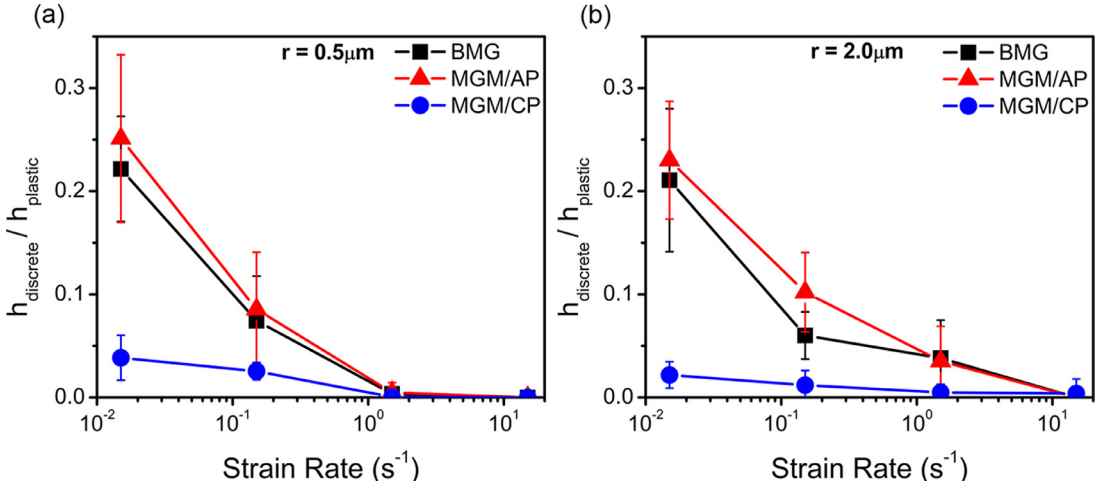

Fig. 10. The propensity for localization as a function of strain rate for indentation of the amorphous (MGM/AP) and crystalline (MGM/CP) phases of the MGM-12Be composite using probe radii of (a) 0.5 and (b) 2.0 μm. Results for the BMG are included for reference.

and R the probe radius [91], the sharper 0.5 μm probe will produce a larger strain beneath the indenter at maximum indentation depths of approximately 450 nm and in turn, greater plastic strain relative to the two larger radius probes. Indeed, the lower strain imparted by the 5.0 μm probe manifested as a rather shallow residual depth for the maximum achievable load of 10 mN, which would inevitably introduce systematic errors into the analysis. Consequently, only the two sharper probes were employed for mapping the propensity for localization as a function of strain rate. Indentation of the crystalline dendrites produced an identical probe size effect as evident in Fig. 9c with two distinguishable features – larger maximum indentation depths due to the reduced hardness of the dendrites relative to the amorphous matrix and loading curves virtually free of displacement bursts with the exception of two discernible events noted for the 0.5 μm probe.

The fraction of discrete plasticity for indents placed deliberately on the amorphous (MGM/AP) and crystalline (MGM/CP) phases of the MGM-12Be composite are shown in Fig. 10a for the 0.5 μm probe. With increasing strain rate, the plastic response of the amorphous phase converged to homogenous flow, in excellent agreement with the behavior of the BMG sample. An analogous trend was uncovered for indents produced with the 2.0 μm probe as shown in Fig. 10b, indicating that the plastic zones produced by both radius probes developed solely within the amorphous phase for the MGM-12Be sample and consistent with the findings in Section 3. The small fraction of discrete plasticity for indents placed deliberately on the crystalline phase in Fig. 10 can be attributed to the plastic zone developing into the amorphous matrix during indentation of the dendrites. Sampling of the combined phase response when specifically indenting the crystalline phase was expected given the larger maximum indentation depths of approximately 600 and 225 nm for the 0.5 and 2.0 μm probes in Fig. 9c, respectively, and the dendrite length scales from Fig. 2a. We also note that the degree of discrete plasticity sampled during indentation of the dendrites can be further enhanced by dislocation slip transfer across the ACIs promoting the activation of STZs as demonstrated by Cheng and Trelewicz [85], which is substantiated by the presence of displacement bursts in loading curve for the 0.5 μm probe noted in Fig. 9c.

Relative to the MGM-12Be sample, the measured characteristic length scale of the amorphous matrix in the MGM-19Be composite was considerably reduced (i.e., 0.43 μm from Table 1). With maximum indentation depths of approximately 0.45 μm for the 0.5 μm probe in Fig. 9b, the plastic zone decidedly expanded into the crystalline phase upon indentation of the amorphous matrix. The reduction in the fraction of discrete plasticity for the amorphous phase in Fig. 11a relative to the response of the MGM-12Be composite can thus be attributed to strain partitioning to the crystalline phase promoting enhanced dislocation plasticity, which will manifest as a more homogenous plastic response. When compared with the BMG, the analogous scaling with strain rate indicates that the same fundamental mechanism involving a shift toward enhanced shear band nucleation are responsible for the transition from incipient to homogenous flow in the amorphous matrix. However,

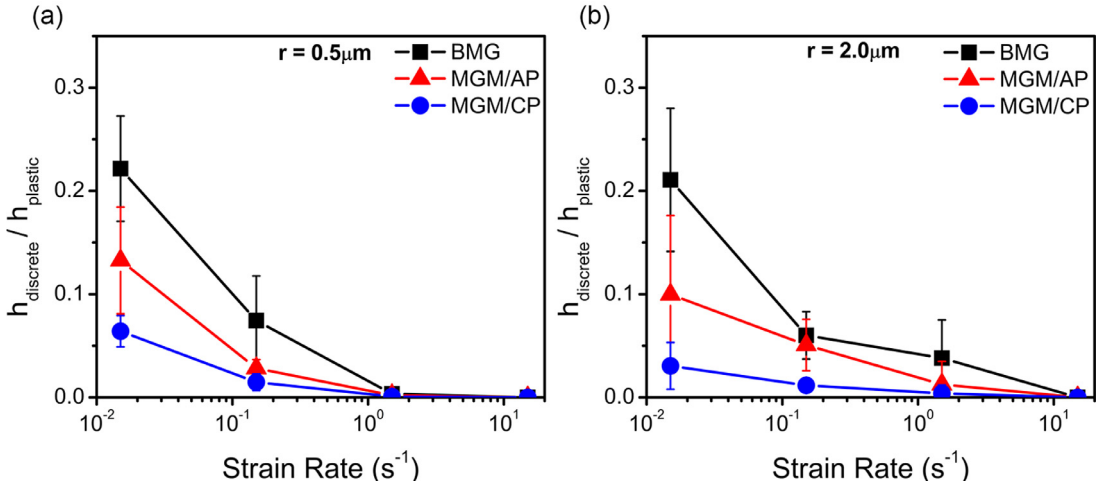

Fig. 11. The propensity for localization as a function of strain rate for indentation of the amorphous (MGM/AP) and crystalline (MGM/CP) phases of the MGM-19Be composite using probe radii of (a) 0.5 and (b) 2.0 μm. Results for the BMG are included for reference.

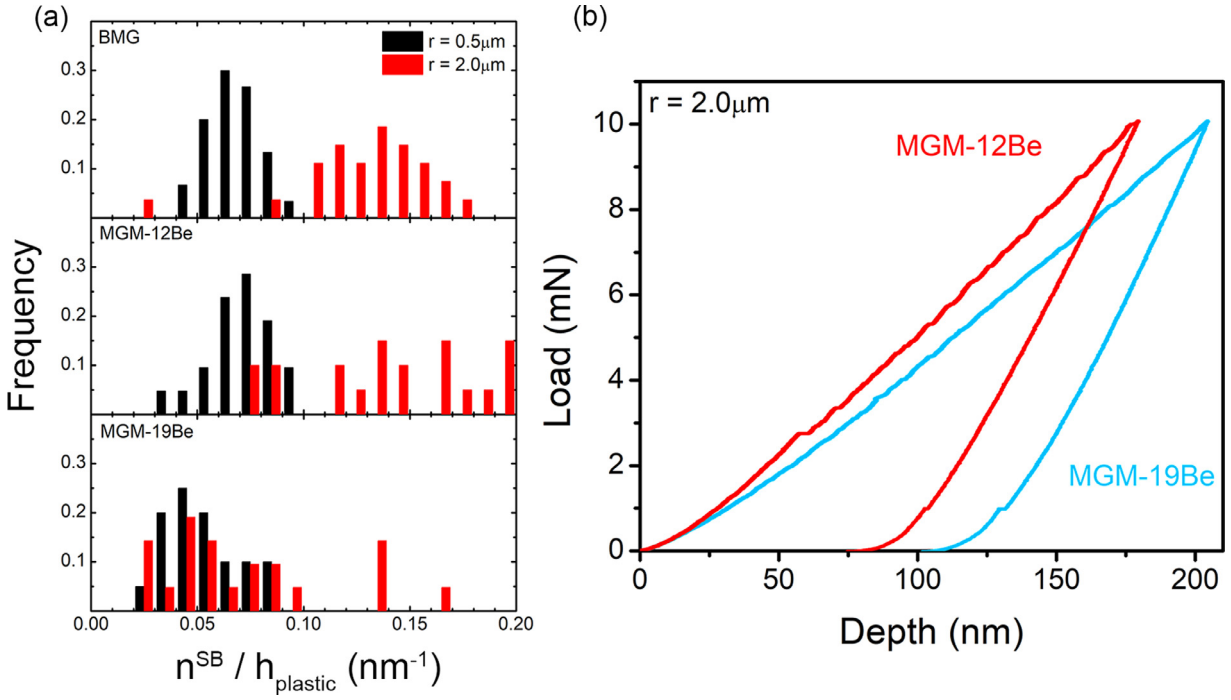

Fig. 12. Distribution of the total number of displacement bursts during loading normalized by the residual plastic depth for the BMG, MGM-12Be, and MGM-19Be samples (from upper to lower panels) for two different probe sizes of 0.5 and 2.0 μm. (b) Representative indentation curves for the MGM-12Be and MGM-19Be samples acquired using the 2.0 μm radius probe demonstrating qualitatively different localization behavior during loading.

the convergence with the response of the crystalline phase at an intermediate strain rate of 0.15 s^{-1} suggests that this transition was influenced by the dendrites arresting shear band growth and in turn, suppressing shear band propagation rates. Further supporting this mechanism was the delay in the convergence with the crystalline response to a higher indentation strain rate of 1.5 s^{-1} for the 2.0 μm probe in Fig. 11b, which is consistent with the reduction in the maximum indentation depth to approximately 0.15 μm for this probe geometry. The fraction of discrete plasticity sampled when indenting the crystalline phase was accentuated relative to the MGM-12Be trends and also attributed to the intrinsically smaller dendrite size in the MGM-19Be composite from Fig. 2a.

To further elucidate the role of ACIs in shear band nucleation and propagation, we translated the different propensity for localization trends into a self-consistent space by plotting distributions of the total number of displacement bursts during loading, n^{SB} normalized by $h_{plastic}$ for the different samples and probe sizes in Fig. 12a. This allows for a direct comparison of the number of distinct shear banding events in the amorphous matrix across the different composites where strain partitioning to the crystalline phase ultimately influences the total plastic depth. Relative to the BMG sample, the normalized number of shear banding events for the MGM-12Be composite closely aligned for the 0.5 μm probe. While the distribution for indents on the same composite from the 2.0 μm probe was broader, its overall range was also comparable with the BMG. Collectively, these results indicate that the mechanical response of the amorphous phase under the selected loading conditions was controlled by shear banding and consistent with all prior findings. For the MGM-19Be composite, the distribution of the normalized number of shear banding events acquired using the 0.5 μm probe was shifted to lower values relative to the BMG. This shift was far more pronounced for the 2.0 μm probe, demonstrating that finer microstruc-

tural length scales promoted a reduction in the number of displacement bursts as the plastic zone expanded into both phases of the composite. The representative loading curve for MGM-19Be sample in Fig. 12b confirms the reduction in the number of detectable displacement bursts and also demonstrates an overall decrease in the average h_i^{SB} relative to the MGM-12Be composite.

In light of the above findings, we can now distinguish between the different mechanisms promoting homogenous flow in MGM composites. First, in the absence of strain partitioning to the crystalline phase, the transition from discrete to homogenous plasticity in the amorphous matrix can be understood through mechanistic analogues of serrated flow studies on metallic glasses to probe the kinetics of shear band nucleation and propagation [92]. With increasing strain rate, shear band propagation rates are not sufficiently fast to relax the surrounding glass, which promotes the nucleation of new shear bands to accommodate strain and manifests as a more homogenous plastic response. Second, under constrained modes of loading when conditions are favorable to distribute strain to both the crystalline and amorphous phases, the reduction in the number of detectable displacement bursts and decrease in the magnitude of individual depth excursions from shear banding collectively indicate that shear band propagation is inhibited by the presence of the crystalline phase. Both biased shear band nucleation due to the ACIs reducing the activation barrier for the onset of shear banding and dendrites arresting propagating shear fronts via strain transfer across the ACI likely contribute to this reduction in the effective shear band propagation rates. Consequently, under unconstrained modes of loading, improvements in mechanical performance will not *only* depend on crystalline phase fraction promoting a transition to dislocation-dominated plasticity, but *also* the extent to which ACIs bias shear band nucleation and propagation rates in the amorphous matrix.

6. Conclusions

Instrumented nanoindentation was employed to study the process of shear delocalization in metallic glasses containing crystalline heterogeneities. By quantifying the state of stress and its implications for the onset of shear banding collectively with the propensity for localization as a function of microstructural length scales, we have identified a convolution of mechanisms that promote homogeneous plastic flow in MGM composites. Our findings are summarized as follows:

i. Strain partitioning to the amorphous and crystalline phases of the composites was quantified through two-dimensional surface hardness mapping combined with statistical through-thickness measurements of mechanical properties as a function of contact depth. The cross-over from individual to combined phase responses was linked to the length scales of the composite microstructure and distinguished from a true composite response, which will exhibit plastic responses influenced by connectivity effects of the composite microstructure.
ii. The shear band nucleation stress at the onset of plasticity in the amorphous matrix was shown to be consistent with a BMG counterpart when the shear plane stress trajectory was confined to the amorphous matrix. However, a discernible reduction in the stress required to nucleate the first shear band in the composite containing the finest microstructural length scales and thus, the greatest interfacial density was demonstrated. This reduction was attributed to the average shear plane stress trajectory intersecting with the ACIs, which indicates that ACIs reduce the activation barrier to nucleate a shear band relative to a monolithic BMG.
iii. When the indentation conditions were favorable to distribute strain to both the crystalline and amorphous phases, enhancing the amount of strain accommodated by the crystalline phase promoted a transition to homogenous flow, which was accompanied by a reduction in the effective shear band propagation rate through the arrestment of propagating shear fronts at the ACIs. Simultaneously, reducing the activation barrier for the onset of shear banding at the ACIs will further enhance homogeneous flow through biased shear band nucleation kinetics.

The improvements in the plastic response of MGM composites relative to their BMG counterparts are thus understood as an interplay between complementary deformation mechanisms involving strain partitioning to the crystalline dendrites, which is accompanied by biased shear band nucleation kinetics and reduced propagation rates in the amorphous matrix. To the extent that shear bands will nucleate at the ACIs, which we have confirmed quantitatively through our experiments, the propensity for shear localization under unconstrained modes of loading will also be dependent on the interface structure and area fraction. Leveraging our knowledge of these synergistic mechanisms will be critical in the design of new MGM composites containing microstructural length scales tailored to balance the effective distribution of plastic strain for inhibiting shear localization in the amorphous matrix and its propagation through the composite microstructure.

Acknowledgments

Support for this work was provided through the National Science Foundation under Award 1401662 with additional support from Award 1554411. The authors gratefully acknowledge the use of electron microscopy resources in the Center for Functional Nanomaterials, which is a US DOE Office of Science Facility at Brookhaven National Laboratory under Contract No. DE- SC0012704. D.C. Hofmann acknowledges support from NASA's Exploration Systems Mission Directorate under Contract no. NNH10ZTT001N. Part of this research was carried out at the Jet Propulsion Laboratory, California Institute of Technology, under contract with NASA.

Declaration of Competing Interest

The authors declare that they have no known competing financial interests or personal relationships that could have appeared to influence the work reported in this paper.

References

[1] A.I. Salimon, M.F. Ashby, Y. Brechet, A.L. Greer, Bulk metallic glasses: what are they good for? Mater. Sci. Eng. A – Struct. Mater. Prop. Microstruct. Process. 375 (2004) 385–388.
[2] M.F. Ashby, A.L. Greer, Metallic glasses as structural materials, Scr. Mater. 54 (3) (2006) 321–326.
[3] A.L. Greer, Metallic glasses ... on the threshold, Mater. Today 12 (1–2) (2009) 14–22.
[4] M.M. Trexler, N.N. Thadhani, Mechanical properties of bulk metallic glasses, Prog. Mater. Sci. 55 (8) (2010) 759–839.
[5] C. Schuh, T. Hufnagel, U. Ramamurty, Mechanical behavior of amorphous alloys, Acta Mater. 55 (12) (2007) 4067–4109.
[6] D. Rodney, A. Tanguy, D. Vandembroucq, Modeling the mechanics of amorphous solids at different length scale and time scale, Model Simul. Mater. Sci. 19 (8) (2011) 083001.
[7] A.S. Argon, Plastic-deformation in metallic glasses, Acta Metall. 27 (1) (1979) 47–58.
[8] A.S. Argon, Mechanisms of inelastic deformation in metallic glasses, J. Phys. Chem. Solids 43 (10) (1982) 945–961.
[9] F. Spaepen, Microscopic mechanism for steady-state inhomogeneous flow in metallic glasses, Acta Metall. 25 (4) (1977) 407–415.
[10] J. Pan, Q. Chen, L. Liu, Y. Li, Softening and dilatation in a single shear band, Acta Mater. 59 (13) (2011) 5146–5158.
[11] E.R. Homer, C.A. Schuh, Three-dimensional shear transformation zone dynamics model for amorphous metals, Model. Simul. Mater. Sci. Eng. 18 (6) (2010) 19.
[12] J.S. Langer, Shear-transformation-zone theory of deformation in metallic glasses, Scr. Mater. 54 (3) (2006) 375–379.
[13] W.D. Liu, H.H. Ruan, L.C. Zhang, On the plasticity event in metallic glass, Philos. Mag. Lett. 93 (3) (2013) 158–165.
[14] T. Egami, Formation and deformation of metallic glasses: atomistic theory, Intermetallics 14 (8) (2006) 882–887.
[15] A.S. Argon, J. Megusar, N.J. Grant, Shear band induced dilations in metallic glasses, Scr. Metall. 19 (5) (1985) 591–596.
[16] E.R. Homer, Examining the initial stages of shear localization in amorphous metals, Acta Mater. 63 (2014) 44–53.
[17] P.S. Steif, F. Spaepen, J.W. Hutchinson, Strain localization in amorphous metals, Acta Metall. 30 (2) (1982) 447–455.

[18] H. Kimura, T. Masumoto, A model of the mechanics of serrated flow in an amorphous alloy, Acta Metall. 31 (2) (1983) 231–240.
[19] F. Shimizu, S. Ogata, J. Li, Yield point of metallic glass, Acta Mater. 54 (16) (2006) 4293–4298.
[20] Y. Fan, T. Iwashita, T. Egami, How thermally activated deformation starts in metallic glass, Nat. Commun. 5 (1) (2014) 5083.
[21] H. Guo, P.F. Yan, Y.B. Wang, J. Tan, Z.F. Zhang, M.L. Sui, E. Ma, Tensile ductility and necking of metallic glass, Nat. Mater. 6 (10) (2007) 735–739.
[22] L.Q. Xing, Y. Li, K.T. Ramesh, J. Li, T.C. Hufnagel, Enhanced plastic strain in Zr-based bulk amorphous alloys, Phys. Rev. B 64 (18) (2001) 4.
[23] D.H. Bae, S.W. Lee, J.W. Kwon, S. Yi, J.S. Park, Deformation behavior of Zr-Al-Cu-Ni-Sn metallic glasses, J. Mater. Res. 21 (5) (2006) 1305–1311.
[24] D.J. Magagnosc, R. Ehrbar, G. Kumar, M.R. He, J. Schroers, D.S. Gianola, Tunable tensile ductility in metallic glasses, Sci. Rep. 3 (2013) 1096.
[25] G.N. Yang, B.A. Sun, S.Q. Chen, J.L. Gu, Y. Shao, H. Wang, K.F. Yao, Understanding the effects of Poisson's ratio on the shear band behavior and plasticity of metallic glasses, J. Mater. Sci. 52 (11) (2017) 6789–6799.
[26] P. Xue, Y.J. Huang, S. Guo, H.B. Fan, Z.L. Ning, J.F. Sun, P.K. Liaw, Understanding the structure-Poisson's ratio relation in bulk metallic glass, J. Mater. Sci. 53 (10) (2018) 7891–7899.
[27] H. Gleiter, Nanoglasses: a new kind of noncrystalline material and the way to an age of new technologies? Small 12 (2016) 2225–2233.
[28] Y. Ivanisenko, C. Kubel, S.H. Nandam, C.M. Wang, X.K. Mu, O. Adjaoud, K. Albe, H. Hahn, Structure and properties of nanoglasses, Adv. Eng. Mater. 20 (12) (2018) 16.
[29] S. Adibi, P.S. Branicio, S.P. Joshi, Suppression of shear banding and transition to necking and homogeneous flow in nanoglass nanopillars, Sci. Rep. 5 (2015) 15611.
[30] J.X. Fang, U. Vainio, W. Puff, R. Würschum, X.L. Wang, D. Wang, M. Ghafari, F. Jiang, J. Sun, H. Hahn, H. Gleiter, Atomic structure and structural stability of Sc75Fe25 nanoglasses, Nano Lett. 12 (1) (2012) 458–463.
[31] N. Chen, D.V. Louzguine-Luzgin, G.Q. Xie, P. Sharma, J.H. Perepezko, M. Esashi, A.R. Yavari, A. Inoue, Structural investigation and mechanical properties of a representative of a new class of materials: nanograined metallic glasses, Nanotechnology 24 (4) (2013) 8.
[32] N. Chen, R. Frank, N. Asao, D.V. Louzguine-Luzgin, P. Sharma, J.Q. Wang, G.Q. Xie, Y. Ishikawa, N. Hatakeyama, Y.C. Lin, M. Esashi, Y. Yamamoto, A. Inoue, Formation and properties of au-based nanograined metallic glasses, Acta Mater. 59 (16) (2011) 6433–6440.
[33] C. Guo, Y. Fang, B. Wu, S. Lan, G. Peng, X.-l. Wang, H. Hahn, H. Gleiter, T. Feng, Ni-P nanoglass prepared by multi-phase pulsed electrodeposition, Mater. Res. Lett. 5 (5) (2017) 293–299.
[34] B. Cheng, J.R. Trelewicz, Controlling interface structure in nanoglasses produced through hydrostatic compression of amorphous nanoparticles, Phys. Rev. Mater. 3 (3) (2019) 9.
[35] O. Adjaoud, K. Albe, Microstructure formation of metallic nanoglasses: insights from molecular dynamics simulations, Acta Mater. 145 (2018) 322–330.
[36] B. Cheng, J.R. Trelewicz, Interfacial plasticity governs strain delocalization in metallic nanoglasses, J. Mater. Res. 34 (13) (2019) 2325–2336.
[37] D. Sopu, Y. Ritter, H. Gleiter, K. Albe, Deformation behavior of bulk and nanostructured metallic glasses studied via molecular dynamics simulations, Phys. Rev. B 83 (10) (2011) 4.
[38] S. Adibi, P.S. Branicio, Y.-.W. Zhang, S.P. Joshi, Composition and grain size effects on the structural and mechanical properties of Cuzr nanoglasses, J. Appl. Phys. 116 (4) (2014) 043522.
[39] X.L. Wang, F. Jiang, H. Hahn, J. Li, H. Gleiter, J. Sun, J.X. Fang, Plasticity of a scandium-based nanoglass, Scr. Mater. 98 (2015) 40–43.
[40] C.A. Schuh, T.G. Nieh, A nanoindentation study of serrated flow in bulk metallic glasses, Acta Mater. 51 (1) (2003) 87–99.
[41] O. Adjaoud, K. Albe, Influence of microstructural features on the plastic deformation behavior of metallic nanoglasses, Acta Mater. 168 (2019) 393–400.
[42] Q.P. Cao, J.W. Liu, K.J. Yang, F. Xu, Z.Q. Yao, A. Minkow, H.J. Fecht, J. Ivanisenko, L.Y. Chen, X.D. Wang, S.X. Qu, J.Z. Jiang, Effect of pre-existing shear bands on the tensile mechanical properties of a bulk metallic glass, Acta Mater. 58 (4) (2010) 1276–1292.
[43] H. Shao, Y.L. Xu, B. Shi, C.S. Yu, H. Hahn, H. Gleiter, J.G. Li, High density of shear bands and enhanced free volume induced in Zr70Cu20Ni10 metallic glass by high-energy ball milling, J. Alloy Compd. 548 (2013) 77–81.
[44] M.H. Lee, K.S. Lee, J. Das, J. Thomas, U. Kuhn, J. Eckert, Improved plasticity of bulk metallic glasses upon cold rolling, Scr. Mater. 62 (9) (2010) 678–681.
[45] T.C. Hufnagel, C. Fan, R.T. Ott, J. Li, S. Brennan, Controlling shear band behavior in metallic glasses through microstructural design, Intermetallics 10 (11–12) (2002) 1163–1166.
[46] E.S. Park, D.H. Kim, Design of bulk metallic glasses with high glass forming ability and enhancement of plasticity in metallic glass matrix composites: a review, Met. Mater. – Int. 11 (1) (2005) 19–27.
[47] D.C. Hofmann, W.L. Johnson, Improving ductility in nanostructured materials and metallic glasses: three laws, in: Y. Zhao, X. Liao (Eds.), Ductility of Bulk Nanostructured Materials, Trans Tech Publications Ltd, Stafa-Zurich, 2010, pp. 657–663.
[48] J. Qiao, H. Jia, P.K. Liaw, Metallic glass matrix composites, Mater. Sci. Eng.: R: Rep. 100 (2016) 1–69.
[49] D.K. Balch, E. Ustundag, D.C. Dunand, Elasto-plastic load transfer in bulk metallic glass composites containing ductile particles, Metall. Mater. Trans. A – Phys. Metall. Mater. Sci. 34A (9) (2003) 1787–1797.
[50] H. Choi-Yim, W.L. Johnson, Bulk metallic glass matrix composites, Appl. Phys. Lett. 71 (26) (1997) 3808–3810.
[51] H. Choi-Yim, R. Busch, U. Koster, W.L. Johnson, Synthesis and characterization of particulate reinforced Zr57Nb5Al10Cu15.4Ni12.6 bulk metallic glass composites, Acta Mater. 47 (8) (1999) 2455–2462.
[52] R.D. Conner, H. Choi-Yim, W.L. Johnson, Mechanical properties of Zr57Nb5Al10Cu15.4Ni12.6 metallic glass matrix particulate composites, J. Mater. Res. 14 (8) (1999) 3292–3297.
[53] A.L. Greer, Partially or fully devitrified alloys for mechanical properties, Mater. Sci. Eng. A – Struct. Mater. Prop. Microstruct. Process. 304 (2001) 68–72.
[54] H. Choi-Yim, R.D. Conner, F. Szuecs, W.L. Johnson, Processing, microstructure and properties of ductile metal particulate reinforced Zr57Nb5Al10CU15.4Ni12.6 bulk metallic glass composites, Acta Mater. 50 (10) (2002) 2737–2745.
[55] R.B. Dandliker, R.D. Conner, W.L. Johnson, Melt infiltration casting of bulk metallic-glass matrix composites, J. Mater. Res. 13 (10) (1998) 2896–2901.
[56] C. Fan, R.T. Ott, T.C. Hufnagel, Metallic glass matrix composite with precipitated ductile reinforcement, Appl. Phys. Lett. 81 (6) (2002) 1020–1022.
[57] J. Eckert, J. Das, S. Pauly, C. Duhamel, Mechanical properties of bulk metallic glasses and composites, J. Mater. Res. 22 (2) (2007) 285–301.
[58] J.B. Li, J.S.C. Jang, S.R. Jian, K.W. Chen, J.F. Lin, J.C. Huang, Plasticity improvement of ZrCu-based bulk metallic glass by ex situ dispersed ta particles, Mater. Sci. Eng. A – Struct. Mater. Prop. Microstruct. Process 528 (28) (2011) 8244–8248.
[59] K. Hajlaoui, A.R. Yavari, A. LeMoulec, W.J. Botta, F.G. Vaughan, J. Das, A.L. Greer, A. Kvick, Plasticity induced by nanoparticle dispersions in bulk metallic glasses, J. Non-Cryst. Solids 353 (3) (2007) 327–331.
[60] K. Albe, Y. Ritter, D. Sopu, Enhancing the plasticity of metallic glasses: shear band formation, nanocomposites and nanoglasses investigated by molecular dynamics simulations, Mech. Mater. 67 (2013) 94–103.
[61] T. Brink, M. Peterlechner, H. Rosner, K. Albe, G. Wilde, Influence of crystalline nanoprecipitates on shear-band propagation in Cu-Zr-based metallic glasses, Phys. Rev. Appl. 5 (5) (2016) 16.
[62] A. Tlili, S. Pailhès, R. Debord, B. Ruta, S. Gravier, J.J. Blandin, N. Blanchard, S. Gomès, A. Assy, A. Tanguy, V.M. Giordano, Thermal transport properties in amorphous/nanocrystalline metallic composites: a microscopic insight, Acta Mater. 136 (2017) 425–435.
[63] C.C. Hays, C.P. Kim, W.L. Johnson, Microstructure controlled shear band pattern formation and enhanced plasticity of bulk metallic glasses containing *in situ* formed ductile phase dendrite dispersions, Phys. Rev. Lett. 84 (13) (2000) 2901–2904.
[64] F. Szuecs, C.P. Kim, W.L. Johnson, Mechanical properties of Zr56.2Ti13.8Nb5.0Cu6.9Ni5.6Be12.5 ductile phase reinforced bulk metallic glass composite, Acta Mater. 49 (9) (2001) 1507–1513.
[65] H. Tan, Y. Zhang, Y. Li, Synthesis of La-based in-situ bulk metallic glass matrix composite, Intermetallics 10 (11–12) (2002) 1203–1205.
[66] U. Kuhn, J. Eckert, N. Mattern, L. Schultz, ZrNbCuNiAl bulk metallic glass matrix composites containing dendritic bcc phase precipitates, Appl. Phys. Lett. 80 (14) (2002) 2478–2480.
[67] G. He, J. Eckert, W. Loser, L. Schultz, Novel Ti-base nanostructure-dendrite composite with enhanced plasticity, Nat. Mater. 2 (1) (2003) 33–37.
[68] M.L. Lee, Y. Li, C.A. Schuh, Effect of a controlled volume fraction of dendritic phases on tensile and compressive ductility in La-based metallic glass, Acta Mater. 52 (14) (2004) 4121–4131.
[69] D. Sorensen, J. Pischlar, J. Stevick, E. Hintsala, D. Stauffer, J.C. Myers, T. Keenan, A.J. Ramirez, Investigation of a dissimilar vitreloy 105 to grade 2 titanium laser weld, Mater. Sci. Eng.: A 742 (2019) 33–43.
[70] Y.S. Oh, C.P. Kim, S. Lee, N.J. Kim, Microstructure and tensile properties of high-strength high-ductility Ti-based amorphous matrix composites containing ductile dendrites, Acta Mater. 59 (19) (2011) 7277–7286.
[71] Y.A. Wu, Y.H. Xiao, G.L. Chen, C.T. Liu, Z.P. Lu, Bulk metallic glass composites with transformation-mediated work-hardening and ductility, Adv. Mater. 22 (25) (2010) 2770.
[72] D.C. Hofmann, J.Y. Suh, A. Wiest, G. Duan, M.L. Lind, M.D. Demetriou, W.L. Johnson, Designing metallic glass matrix composites with high toughness and tensile ductility, Nature 451 (7182) (2008) 1085–10U3.
[73] X.L. Fu, Y. Li, C.A. Schuh, Mechanical properties of metallic glass matrix composites: effects of reinforcement character and connectivity, Scr. Mater. 56 (7) (2007) 617–620.
[74] R.L. Narayan, P.S. Singh, D.C. Hofmann, N. Hutchinson, K.M. Flores, U. Ramamurty, On the microstructure-tensile property correlations in bulk metallic glass matrix composites with crystalline dendrites, Acta Mater. 60 (13–14) (2012) 5089–5100.
[75] W.C. Oliver, G.M. Pharr, An improved technique for determining hardness and elastic modulus using load and displacement sensing indentation experiments, J. Mater. Res. 7 (6) (1992) 1564–1583.
[76] E.D. Hintsala, U. Hangen, D.D. Stauffer, High-throughput nanoindentation for statistical and spatial property determination, JOM 70 (4) (2018) 494–503.
[77] C.A. Schuh, Nanoindentation studies of materials, Mater. Today 9 (5) (2006) 32–40.
[78] C.E. Packard, C.A. Schuh, Initiation of shear bands near a stress concentration in metallic glass, Acta Mater. 55 (16) (2007) 5348–5358.
[79] J.L. Cheng, G. Chen, F. Xu, Y.L. Du, Y.S. Li, C.T. Liu, Correlation of the microstructure and mechanical properties of Zr-based in-situ bulk metallic glass matrix composites, Intermetallics 18 (12) (2010) 2425–2430.
[80] N. Van Steenberge, J. Sort, A. Concustell, J. Das, S. Scudino, S. Surinach, J. Eckert, M.D. Baro, Dynamic softening and indentation size effect in a Zr-based bulk glass–forming alloy, Scr. Mater. 56 (7) (2007) 605–608.
[81] S. Wang, Y.F. Ye, B.A. Sun, C.T. Liu, S.Q. Shi, Y. Yang, Softening-induced plastic flow instability and indentation size effect in metallic glass, J. Mech. Phys. Solids 77 (2015) 70–85.

[82] F.Q. Yang, K.B. Geng, P.K. Liaw, G.J. Fan, H. Choo, Deformation in a Zr57Ti5CU20Ni8Al10 bulk metallic glass during nanoindentation, Acta Mater. 55 (1) (2007) 321–327.
[83] J.-i. Jang, B.-.G. Yoo, Y.-.J. Kim, J.-.H. Oh, I.-.C. Choi, H. Bei, Indentation size effect in bulk metallic glass, Scr. Mater. 64 (8) (2011) 753–756.
[84] R.L. Narayan, K. Boopathy, I. Sen, D.C. Hofmann, U. Ramamurty, On the hardness and elastic modulus of bulk metallic glass matrix composites, Scr. Mater. 63 (7) (2010) 768–771.
[85] B. Cheng, J.R. Trelewicz, Mechanistic coupling of dislocation and shear transformation zone plasticity in crystalline-amorphous nanolaminates, Acta Mater. 117 (2016) 293–305.
[86] Y.M. Wang, J. Li, A.V. Hamza, T.W. Barbee, Ductile crystalline-amorphous nanolaminates, Proc. Natl. Acad. Sci. USA 104 (27) (2007) 11155–11160.
[87] B. Cheng, J.R. Trelewicz, Design of crystalline-amorphous nanolaminates using deformation mechanism maps, Acta Mater. 153 (2018) 314–326.
[88] B. Moser, J.F. Loffler, J. Michler, Discrete deformation in amorphous metals: an *in situ* SEM indentation study, Philos. Mag. 86 (33–35) (2006) 5715–5728.
[89] I.C. Choi, Y. Zhao, Y.J. Kim, B.G. Yoo, J.Y. Suh, U. Ramamurty, J.I. Jang, Indentation size effect and shear transformation zone size in a bulk metallic glass in two different structural states, Acta Mater. 60 (19) (2012) 6862–6868.
[90] C. Liu, P. Guan, Y. Fan, Correlating defects density in metallic glasses with the distribution of inherent structures in potential energy landscape, Acta Mater. 161 (2018) 295–301.
[91] D. Tabor, The Hardness of Metals, Oxford University Press, 2000.
[92] C.A. Schuh, A.C. Lund, T.G. Nieh, New regime of homogeneous flow in the deformation map of metallic glasses: elevated temperature nanoindentation experiments and mechanistic modeling, Acta Mater. 52 (20) (2004) 5879–5891.